Icarus 226 (2013) 522–535

Contents lists available at SciVerse ScienceDirect

Icarus

journal homepage: www.elsevier.com/locate/icarus

Saturn's thermal emission at 2.2-cm wavelength as imaged by the Cassini RADAR radiometer

M.A. Janssen [a,*], A.P. Ingersoll [b], M.D. Allison [c], S. Gulkis [a], A.L. Laraia [b], K.H. Baines [a], S.G. Edgington [a], Y.Z. Anderson [a], K. Kelleher [a], F.A. Oyafuso [a]

[a] Jet Propulsion Laboratory, California Institute of Technology, Pasadena, CA, 91109, United States
[b] California Institute of Technology, Pasadena, CA, 91125, United States
[c] NASA Goddard Institute for Space Studies, New York, NY, 10025, United States

ARTICLE INFO

Article history:
Available online 21 June 2013

Keywords:
Saturn, Atmosphere
Atmospheres, Structure
Atmospheres, Composition
Radiative transfer
Radio observations

ABSTRACT

We present well-calibrated, high-resolution maps of Saturn's thermal emission at 2.2-cm wavelength obtained by the Cassini RADAR radiometer through the Prime and Equinox Cassini missions, a period covering approximately 6 years. The absolute brightness temperature calibration of 2% achieved is more than twice better than for all previous microwave observations reported for Saturn, and the spatial resolution and sensitivity achieved each represent nearly an order of magnitude improvement. The brightness temperature of Saturn in the microwave region depends on the distribution of ammonia, which our radiative transfer modeling shows is the only significant source of absorption in Saturn's atmosphere at 2.2-cm wavelength. At this wavelength the thermal emission comes from just below and within the ammonia cloud-forming region, and yields information about atmospheric circulations and ammonia cloud-forming processes. The maps are presented as residuals compared to a fully saturated model atmosphere in hydrostatic equilibrium. Bright regions in these maps are readily interpreted as due to depletion of ammonia vapor in, and, for very bright regions, below the ammonia saturation region. Features seen include the following: a narrow equatorial band near full saturation surrounded by bands out to about 10° planetographic latitude that demonstrate highly variable ammonia depletion in longitude; narrow bands of depletion at −35° latitude; occasional large oval features with depleted ammonia around −45° latitude; and the 2010–2011 storm, with extensive saturated and depleted areas as it stretched halfway around the planet in the northern hemisphere. Comparison of the maps over time indicates a high degree of stability outside a few latitudes that contain active regions.

1. Introduction

The thermal emission from the gas giant planets was first observed by single-antenna telescopes in the 1950s (Mayer et al., 1958), and quantitatively related to fundamental atmospheric properties in the following decade (Thornton and Welch, 1963; Gulkis et al., 1969; Wrixon and Welch, 1970). Subsequent observations through the 1980s filled in the disk-temperature spectra of Jupiter and Saturn through the millimeter- and centimeter-wavelength range. This combined with advances in understanding the high-pressure microwave absorption of ammonia, which possesses a strong inversion band just longward of 1-cm wavelength, led to a consistent story of deeply convective atmospheres with ammonia as the dominant absorber (Gulkis and Poynter, 1972; Berge and Gulkis, 1976; Klein and Gulkis, 1978). The whole disk spectrum through the microwave region for Saturn led to a value for the deep atmosphere mixing ratio of ammonia of about three times the solar abundance, value consistent with previous work (de Pater, 1990; Atreya, 2010), and our analysis in L13. The measured disk temperature spectrum of Saturn may be found in de Pater and Massie (1985) and van der Tak et al. (1999).

The advent around the same time of radio interferometers capable of using aperture synthesis to image the planets led to the first microwave image of Saturn, reported by Schloerb et al. (1979) using the interferometer Owens Valley Radio Observatory at 3.7-cm wavelength. The completion of the National Radio Astronomical Observatory's Very Large Array in New Mexico was followed by a series of images of Saturn and its rings made with this instrument reported by a number of authors at wavelengths ranging from 2- to 21-cm wavelength (e.g., de Pater and Dickel, 1982, 1991; Grossman et al., 1989; Grossman, 1990). These studies have resulted in a better understanding of Saturn's rings and atmospheric microwave spectrum, and have provided evidence of large-scale structure in Saturn's ammonia distribution including variable broad bands in the midlatitudes. However, they have been

* Corresponding author. Fax: +1 818 354 8895.
E-mail address: michael.a.janssen@jpl.nasa.gov (M.A. Janssen).

0019-1035/$ - see front matter © 2013 Elsevier Inc. All rights reserved.
http://dx.doi.org/10.1016/j.icarus.2013.06.008

Table 1
Nominal radiometer characteristics.

Frequency	13.78 GHz
Wavelength	2.18 cm
Polarization	One linear
Radiometer bandpass	135 MHz
Measurement noise	0.026 K/$\sqrt{}$Hz
Beam full width at half-power (beam 3)	0.36° Circular

limited by the capabilities of the VLA in spatial resolution and dynamic range for imaging extended objects, in addition to which the process of Earth-rotational aperture synthesis used for imaging averages out longitudinal structure. The theoretical capability for the synthesized beam of the VLA in its largest (D) configuration is 1.3″ at 2-cm wavelength, providing spatial resolution on Saturn comparable to that achieved here (1° latitude at the equator). However, results published to date show actual spatial resolutions achieved to be 6° or greater in latitude (e.g., Grossman et al., 1989; van der Tak et al., 1999; Dunn et al., 2002).

The presence of a microwave radiometer in orbit around Saturn provides a unique opportunity to image Saturn with the advantage of close range and without the limitations of a ground-based approach. In this paper we present global maps of Saturn obtained over the course of the Cassini prime and equinox missions by the radiometer that is incorporated into the Cassini RADAR instrument. The emphasis in this paper is to describe the observations, the mapping approach, and overall interpretations. We describe the observational approach and calibration in the next section. In Section 3 we concentrate on the generation of the maps and their interpretation in terms of the ammonia distribution, followed by a discussion of the nature and magnitude of residual errors in the maps. We pay particular attention to the latter since the mapping approach is unique. In Section 4 we offer a discussion and general interpretation of the features seen in the maps, leaving a more detailed discussion of the broader implications to a companion paper by Laraia et al. (2013), henceforth referred to as L13.

2. Observations

2.1. The Cassini radiometer

The Cassini RADAR instrument includes a radiometer that obtains measurements of externally generated (passive) radiation entering the receiver in all operating modes of the instrument, including the various radar modes during which internally-generated (active, or radar) signals are transmitted (Elachi et al., 2004; West et al., 2009; Janssen et al., 2009). The overall characteristics of the radiometer are given in Table 1. The RADAR instrument operates in repetitive "burst" cycles, in which each cycle is divided into active (radar transmit/receive) and passive (radiometer) segments. The radiometer segment employs a Dicke-switching technique in which the noise power received through the antenna is compared with that from an internal reference blackbody termination using a microwave switch to select either the external (sky) signal or an internal reference, using the comparison to stabilize the sky signal. In general operation a second switch is used to select among an array of five antenna feeds; e.g., cycling through these enable synthetic aperture radar observations to be obtained in a wide swath. The duration of the transmit/receive period is adjustable, as are the number and duration of the radiometer averaging intervals. In the Saturn observations we used a 1-s duration burst cycle in which the active segment was eliminated and the antenna was set to the central (and smallest) radar beam, beam 3. The radiometric segment was expanded to observe the target for the entire 1-s period except for a 25 ms integration on the reference load in each cycle, These choices provided the beamwidth and sensitivity given in Table 1.

2.2. Observational approach

The RADAR radiometer was used to observe Saturn during five equatorial periapsis passes occurring between 2005 and 2011 for the purpose of mapping its 2.2-cm thermal emission. The dates and general orbital parameters for these observations are given in Table 2, and details helpful for the interpretation of the maps are given in Table 3. The observations were centered approximately on the periapsis of each pass in order to obtain the best achievable spatial resolution, which is important given that the 0.36° beamwidth of the radiometer is large compared to the resolutions of typical imaging instruments. Saturn presents a challenge comparable to that of Titan for mapping and calibration – it is an extended source that requires a large number of individual observations to build an image, each of which must be corrected for gain and baseline drift as well as signal contamination by sidelobe contributions. The approach developed for Titan for calibration and sidelobe contribution removal was carried over directly to Saturn and is described further below. The actual mapping strategy was necessarily different than the raster scanning and long-term mosaicking approach used on Titan, however, because of the different spacecraft trajectories relative to the target and Saturn's rapidly changing surface structure. Our approach for Saturn was to scan repetitively from pole to pole through Saturn's nadir as rapidly as practical as the spacecraft moved along its trajectory through periapsis, letting the motion of the spacecraft combined with Saturn's rotation provide the westward longitudinal component of the scan. Each scan took from five to ten minutes depending on range, during which time the subspacecraft longitude increased somewhat more than a beamwidth. This led to a spatial asymmetry in sampling discussed further below. Fig. 1 shows both the scan pattern of the beam axis in inertial space as it progressed with time, and as a track on the surface of Saturn, where we take the December 2009 pass as an example (the underlying map is derived from the data as described later in this paper). The gap at approximately 11 h (25° west longitude in the lower panel) was caused by the need to unload the spacecraft momentum wheels. In the lower

Table 2
Mapping orbit characteristics.

Date	Start time (UT)	Segments	Mapping duration (h)	S/C orbit inclination relative to Saturn (°)	Ring plane crossing longitude (°W Lon.)	Periapsis	
						Distance (R_S)	Saturn longitude (°W Lon.)
September 23, 2005	2005 SEP 23 11:15	3	22.78	0.32	–	2.002	298.3
October 13, 2009	2009 OCT 13 23:26	4	11.83	0.55	190.5	2.198	148.5
December 09, 2009	2009 DEC 09 22:58	2	13.94	0.50	18.1	2.220	313.9
July 24, 2010	2010 JUL 24 22:15	2	12.90	4.66	282.1	2.475	312.7
March 20, 2011	2011 MAR 20 04:03	1	14.08	0.38	–	3.722	257.8

Table 3
Mapping details.

Date	Segment number	Relative time from start		Range		Ring inclination seen from S/C		Equatorial longitude scan spacing		Equatorial latitude beam footprint		S/C rotation axis (X/Y)	Orientation of 2nd to Saturn pole (N/S)
		Begin (h)	End (h)	Begin (R_S)	End (R_S)	Begin (°)	End (°)	Min (°)	Max (°)	Min (°)	Max (°)		
September 23, 2005	1	0	4.22	6.70	4.43	0.179	0.76	2.57	2.80	1.91	2.86	X	S
	2	4.97	12.55	2.69	2.45	−0.111	−0.278	1.50	2.32	0.86	1.16	X	S
	3	20.68	22.46	6.72	7.75	0.010	0.042	2.37	2.48	2.89	3.33	X	S
October 13, 2009	1	0	3.34	4.22	2.74	0.420	0.544	2.54	3.13	1.81	1.18	Y	S
	2	3.77	7.15	2.50	2.36	0.544	0.211	1.96	2.33	0.95	1.08	Y	S
	3	7.49	10.54	2.50	3.75	0.128	−0.224	2.44	3.12	1.08	1.61	Y	S
	4	10.96	11.83	4.04	4.41	−0.265	−0.310	2.96	3.12	1.74	1.90	Y	N
December 09, 2009	1	0	10.95	4.93	3.26	0.229	0.001	1.98	2.98	0.95	2.12	Y	S
	2	11.24	13.95	3.52	4.58	−0.051	−0.195	2.83	3.11	1.61	1.98	Y	N
July 24, 2010	1	0	11.29	2.79	4.60	2.788	−4.252	2.10	3.05	1.05	1.97	Y	S
	2	11.49	12.90	4.86	5.35	−4.128	−3.897	3.01	3.12	2.09	2.32	Y	N
March 20, 2011	1	0	14.08	5.64	5.12	0.049	0.261	2.66	2.93	1.60	2.41	Y	S

panel the mapping began at approximately 165° west longitude and proceeded westward. Each 1-s measurement is plotted as a single point.

Each scan crossed the limb onto cold sky (i.e., empty space with the approximately 2.7 K brightness temperature of the cosmic background), moving off the disk by a few beamwidths at each pole to enable the radiometric baseline determination described below. The net angular dimension of the pole-to-pole scan on the sky had to grow and shrink with time to follow Saturn's apparent diameter from the perspective of the spacecraft. In our operational sequence this dimension was readjusted only for a few scans at a time, leading to a sawtooth appearance in the off-disk data seen in later figures. The scanning was achieved using the spacecraft momentum wheels, accelerating and decelerating the spacecraft around one of its axes at the fastest possible rate (the respective spacecraft axes used for each observational segment are given in Table 3).

The 1-s integration time of the radiometer led to oversampling in latitude for all observations, but the limitations on spacecraft angular velocity using momentum wheels generally resulted in an undersampling in longitude. Fig. 2 illustrates this, showing the half-power beam footprints for two partial maps of Saturn that represent the highest (left) and lowest (right) spatial resolution achieved among all the observations. Both maps are from the September 2005 campaign (see Fig. 9). The brightness in latitude is actually oversampled – for clarity only every fourth footprint in latitude is shown here. The undersampling in longitude is real, however, and is unavoidable because of constraints on the spacecraft slew rate. The gap from 0° to 20° latitude in the scan at 298° is due to missing data and is filled in by interpolation in the image (this is the only such case for all the maps). Planetographic latitudes are used here and throughout except where explicitly noted. Table 3 illustrates that the variable geometrical aspects of the scanning conspired to give a fairly regular longitudinal spacing, in the approximate range 2–3° throughout. All of the mapping campaigns except that in 2011 were interrupted by the need to halt the scan to unwind the momentum wheels or, in the 2005 pass, to accommodate another observation as well. These pauses led to significant gaps in longitudinal coverage in all but the 2011 map.

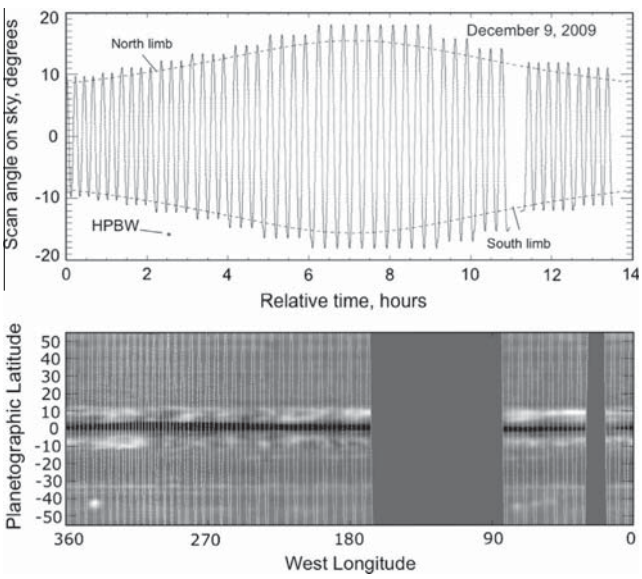

Fig. 1. Scan pattern of the radiometer for a mapping campaign in 2009, in inertial space and time (upper panel), and as tracks on the surface of Saturn (lower panel). The underlying map is derived from the data as described later in this paper. The 0.36° half-power beamwidth (HPBW) is shown in the upper panel for reference.

2.3. Calibration

The primary target for the RADAR instrument, including its radiometer, has been the surface of Saturn's moon Titan. The overall approach for radiometric observation and calibration used for Saturn in this paper was developed originally using Titan observations made through the period October 2004 to May 2007, as described by Janssen et al. (2009, henceforth referred to as J09). We have continued this effort through to the present, using a database on Titan that has now more than doubled. The approach is briefly summarized here. The radiometer provides an output signal (e.g., a voltage) that is proportional to the radiant power entering the radiometer within its 235 MHz bandpass (see Table 1). Both a cold and warm reference are required to determine a calibration factor that converts this output to radiance in appropriate units, which in the microwave region is brightness temperature in units of degrees Kelvin, or the temperature of a blackbody with equivalent radiance. This scale is effectively linear with radiant power since the microwave region is deep in the Rayleigh–Jeans regime of the Planck function, with differences that are negligible in the present study. Observation of cold sky (i.e., 2.7 K) provides the low-temperature reference, or baseline, while a source of known radiance is typically used to provide the high-temperature reference. The calibration factor, or gain, and the baseline both drift with time. For example, gain variations are caused by instrument thermal

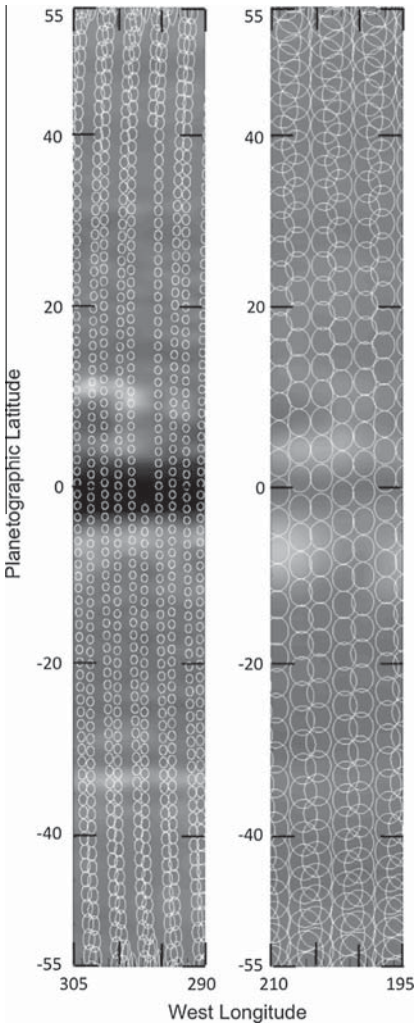

Fig. 2. Beam footprints on Saturn at two extremes of resolution. Shown are the half-power beam footprints on two partial maps of Saturn from September 2005.

variations resulting from instrument warm up after turn on as well as variations in the observing geometry and consequent solar illumination of the instrument during the course of the observations. Such variations also affect the baseline. Observations of cold sky obtained by moving off source from time to time enable the baseline drift to be tracked, while frequent views of our internal reference load allows relative gain variations to be tracked.

The absolute calibration, or the conversion of output voltage to radiometric brightness temperature in units of degrees Kelvin, must be independently obtained, and we used Titan for this purpose. During the period covered by J09, Titan was observed by the RADAR radiometer in 69 individual observing segments during 18 flybys of Titan by the Cassini spacecraft, at a variety of geometries and polarizations covering most of Titan, and at distances ranging from 1000 to 100,000 km. Global map mosaics of effective dielectric constant were determined from the measured thermal polarization. These enabled the construction of global maps of equivalent brightness temperature at normal incidence. We showed that the emissivity could be reliably predicted to better than 1% in special regions such as the dune fields and methane seas, which allowed us to make an absolute calibration of the brightness based on the measured physical temperature of the surface from the Huygens lander (93.7 K, Fulchignoni et al., 2005). In addition to the increased database of Titan observations, our physical reference temperature is now supplemented by extensive infrared surface temperature measurements by the Cassini Composite Infrared Spectrometer (CIRS, Jennings et al., 2009; Cottini et al., 2012), which we used to develop a seasonal surface temperature model for Titan's entire surface. This work will be reported in a future paper; however, we note here that the net calibration scale change from the J09 paper amounted to only about 0.5%.

Knowledge of the beam pattern is essential to construct absolute maps from the observations. The pattern of the circular central beam has been measured by scanning the Sun's emission to an accuracy of one part in 10^4 out to 2° from the boresight as described in J09. However, the sidelobes out to as far as 60° are responsible for a large additional signal, particularly at close range where the disk of Titan fills a significant fraction of the forward hemisphere; e.g., at close range the contribution of sidelobes outside 2° amount to nearly 30% of the main beam signal! These sidelobes were never measured in the ground calibrations and were unknown before the Titan observations; however, we solved for them as a byproduct of the mapping. Their knowledge allowed us to compute and remove this error signal for all Titan observations to within better than 1% of the main beam signal. Our solution was used for Saturn, which presents the same problem.

Finally, we consider that the gain of the radiometer may change in the long term over time, as for example might be expected due to aging of receiver components. Hence we included the determination of a slow linear drift of the gain in the Titan calibration over years. Although Titan was the reference used for this in the J09 calibration, we found that it was better determined from the present Saturn observations themselves. These considerations along with detailed error estimates are discussed following the presentation of the maps in the next section.

3. Mapping Saturn

3.1. Emission model

The results presented in this paper are given as maps of brightness temperature relative to brightness temperatures computed for an assumed model for Saturn's structure and ammonia distribution. The radiative transfer calculations used for this comparison rely on a computer program currently under development for the Juno Microwave Radiometer (MWR) experiment at Jupiter (Janssen et al., 2005, in preparation). This program, called the Juno Atmospheric Microwave Radiative Transfer (JAMRT) program, constructs model atmospheres and carries out radiative transfer calculations at microwave frequencies. This program was written specifically to support the Juno mission to Jupiter, but it is equally useful for the analysis of the Saturn observations reported here when the physical parameters and composition appropriate for Saturn are substituted for those of Jupiter.

The model atmosphere part of the JAMRT program builds deep convective models, including dry adiabatic lapse rates in the deep atmosphere and wet adiabatic lapse rates in the cloud forming regions. The release of heat in the ortho–para transition of H_2, assumed to be in equilibrium in all levels, is included. The gravitational potential is calculated using the equation for the potential function for a fluid having a uniform angular velocity (i.e., Lindal et al., 1985). We use the JPL NASA web site (ssd.jpl.nasa.gov/?gravity_fields_op) to obtain the gravity field data. The gravitational moments are referred to the distance 60,330 km. The radius of Saturn is taken to be 60,268 km. We use a rotation period of 10 h 32 m 35 s. The mass of Saturn in units of GM is taken to be 37,931,208 km^3/s^2. For the purposes of the radiative transfer calculations, we assume the atmosphere be stratified with the normal to the stratified layers following the normal to the equipotential surfaces of Saturn. The reference surface is located at the 1-bar

pressure level with a temperature that is selectable by the user. The full model atmosphere extends over the pressure range from 1000 bars to ~550 mb where the temperature is 110 K. Layer thicknesses are generally taken to be 100 m except in the vicinity of cloud layers, where we reduce the layer thickness to account for the transition that accompanies the formation of the clouds. The dry atmosphere components are H_2, He, CH_4, and the noble gas Argon. The condensable gases are H_2O, H_2S, PH_3 and NH_3. The condensates are H_2O ice, H_2O liquid, NH_3/H_2O solution, NH_4SH ice, and NH_3 ice. The program calculates the depletion of NH_3 both in the water cloud region, due to its absorption into water droplets, and in the ammonium hydrosulfide cloud region due to its interaction with H_2S to form NH_4SH. Vapor pressures and moist adiabats for these gases and condensates are given in Atreya (1986).

The brightness temperature of the atmosphere depends on the distribution of microwave absorbers with temperature. Central to the development of the JAMRT program was an effort, also funded by the Juno project, to better determine the microwave absorption coefficients of the constituents that contribute to Jupiter's thermal microwave emission. The potential absorbers include (1) the polarized gases NH_3, H_2O, PH_3, and H_2S, (2) pressure-induced absorption due to the non-polarized gases that constitute the bulk of the atmosphere, H_2, He, and CH_4, and (3) cloud particles. Gaseous ammonia, as the dominant source of microwave opacity in the gas giant planet atmospheres, has been given the most attention. Its absorption is due primarily to its very strong inversion band centered around 1.4-cm wavelength, and its absorption at longer wavelengths can be modeled as due to the pressure-broadened wings of the lines in this band along with some contribution from infrared rotational transitions. Its absorption coefficient has been measured in H_2–He mixtures over a pressure–temperature range consistent with the atmospheres of the gas giant planets, up to limiting values of 100 bars and 500 K respectively (Hanley et al., 2009; Deveraj, 2011). The data were fit with the help of a Ben-Reuven line-broadening model to produce an empirical expression for the NH_3 absorption coefficient that covers the 1.3–50-cm wavelength range of the Juno experiment. The uncertainty applicable to the 2.2-cm wavelength range for Saturn is estimated to be better than 10% (Hanley et al., 2009).

Our absorption model for PH_3 is based on pressure-broadened rotational transitions using a Van Vleck–Weisskopf lineshape, with absorption consistent with laboratory measurements (Hoffman et al., 2001; Mohammed, 2004). A similar calculation for H_2S is also consistent with laboratory measurements (DeBoer and Steffes, 1994). Although H_2O is a significant source of opacity in the deep atmosphere, it is largely absent from the region responsible for the 2.2-cm emission and of negligible importance here. Our model for H_2O absorption is from Karpowicz and Steffes (2011a, 2011b). Other polarized molecules (e.g., HCN, CN, and CO) are of much lower abundance and are not considered. Cloud NH_3 and NH_4SH ice particle absorption is estimated based on an assumed complex dielectric constant of $4.5 + 3.25 \times 10^{-6}\nu$ (GHz) for particle size $\ll$2.2 cm, a value based on data taken at 1 MHz on NH_3 ice by Lorenz (1998) and highly uncertain, while the absorption of H_2O/NH_3 mixtures in the water cloud region are based on laboratory measurements (Duong, 2011).

The JAMRT program has the capability to compute radiometric brightness temperatures for user-selectable absorber concentrations and cloud properties of condensable species, including their relative humidities in the cloud regions. Table 4 gives an estimate of Saturn's deep atmosphere composition based on values derived from Atreya (2010). Fig. 3 shows the absorption with pressure of the leading absorbers in the atmosphere computed for an atmosphere with this composition, assuming that all condensable species form fully saturated clouds (i.e., 100% relative humidity) with no precipitation. Gaseous ammonia is seen to be by far the dominant absorber in the atmosphere, particularly in the region responsible for the 2.2-cm emission. Phosphine is the next most important absorber above the water cloud region, although with a contribution three or four orders of magnitude less than that of NH_3 in the effective region of emission. H_2S absorption is yet smaller, besides which it effectively disappears in the region where the 2.2-cm emission originates as it combines with NH_3. We note that although H_2S contributes negligibly to the absorption directly, its deep abundance can have a significant impact on the 2.2-cm brightness through this depletion of upper-level ammonia. Other polarized molecules (e.g., HCN, CN, and CO) are of much lower abundance and are not considered. The sum of collision-induced absorption due to H_2, He, and CH_4 collisions is shown (Orton et al., 2007; Birnbaum et al., 1996; Borysow and Frommhold, 1986) and seen to be negligible at our wavelength. The contributions from NH_3 and NH_4SH ice particle shown in the figure are reasonable but rough estimates, but are highly conservative because of the assumption that no precipitation occurs. We consider their possible contributions to be negligible.

The JAMRT program has much flexibility (see L13 for a more general application). In this paper, we take as our standard only the very simple case illustrated in Fig. 4, which assumes the model atmosphere described above with the composition given in Table 4, moist adiabatic temperature lapse rates and full saturation for cloud regions, and a temperature of 134.8 K at the 1-bar pressure level based on the Voyager measurement by Lindal et al. (1985). We use this case as a reference model with which to compare our brightness measurements. Fig. 4 depicts the atmosphere's

Table 4
Composition of the Saturn reference model atmosphere (based on Atreya (2010)).

Constituent	Solar abundance (mixing ratio relative to H_2)	Enrichment of the Saturn atmosphere relative to solar
He	0.195	0.6955
CH_4	5.5×10^{-4}	9.4
H_2O	1.026×10^{-3}	3.0
NH_3	1.352×10^{-4}	3.0
H_2S	3.10×10^{-5}	5.0
Ar	7.24×10^{-6}	1.0
PH_3	5.14×10^{-7}	7.5

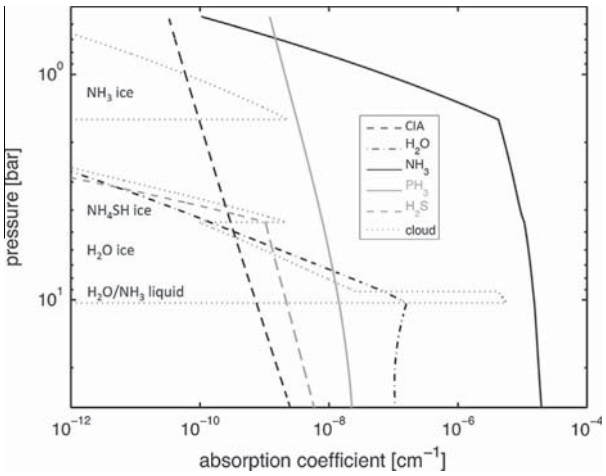

Fig. 3. Microwave absorption profiles at 2-cm wavelength for possible absorbing constituents through the NH_3 cloud region. The atmospheric composition is that of our reference model as given in Table 4. The dotted lines indicate conservative estimates for various particulate absorbers as indicated, while the other lines represent individual gases identified in the legend. The curve labeled CIA includes the sum of H_2–H_2, H_2–He, and H_2–CH_4 collision-induced absorption.

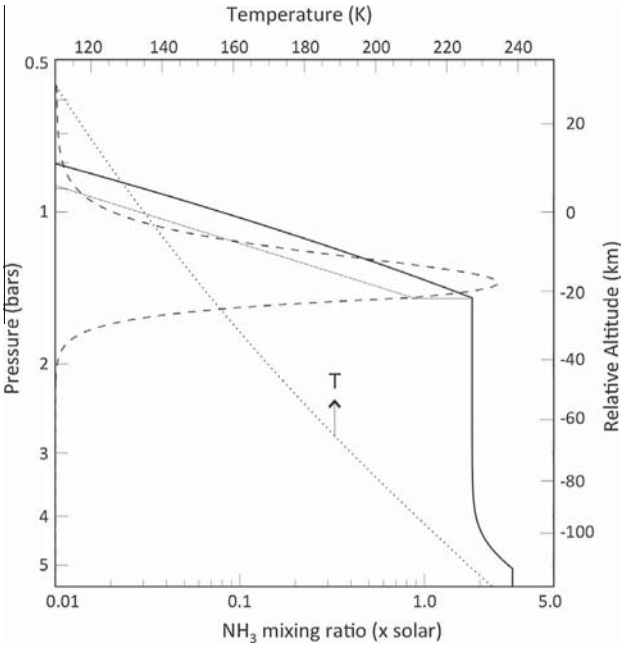

Fig. 4. Atmospheric model used to compute reference brightness temperatures. The temperature (dotted line) and NH_3 mixing ratio in units of solar abundance (thick solid line) are shown as a function of pressure and altitude in the vicinity of the ammonia cloud region in the atmosphere. The reference model assumes 100% relative humidity for ammonia above its saturation level, while the light solid line shows a case for 50% relative humidity. The decrease in NH_3 mixing ratio above the 5-bar level is due to reaction with H_2S to form NH_4SH ice. The dashed line shows the 2.2-cm wavelength weighting function in arbitrary linear units at normal incidence for the reference model.

pressure–temperature relationship along with the ammonia distribution and the corresponding weighting function at 2.2 cm. Note that the ammonia mixing ratio is not constant beneath its nominal saturation level – this is because it is assumed to interact with subcloud H_2S to form ammonium hydrosulfide, which reduces the NH_3 mixing ratio until all of the sulfur is depleted (the loss of NH_3 into water cloud drops is small relative to this). For example, the microwave spectrum has been interpreted to show such a subcloud depletion (Briggs and Sackett, 1989; Grossman, 1990; de Pater et al., 2001). The ammonia concentration above the saturation level is assumed to follow the Clausius–Clapeyron equation, equivalent to the assumption that the cloud region relative humidity is everywhere 100%.

All results in the following are presented as residuals after the subtraction of the reference model brightness values from the measured values, where we take into account both emission angle and latitude dependence in the model for each measurement point. Unless supersaturation is allowed, any plausible redistribution of ammonia in this model for a given deep abundance can only reduce the amount of vapor in the emission region, which lowers the weighting function and results in a higher brightness temperature because of the atmospheric temperature lapse rate. Hence the brightness temperature residuals are expected to all be positive. Since the 2-cm weighting function lies almost entirely within the saturation region in the reference model, the computed brightness temperatures are only weakly dependent on the deep abundance of ammonia. Further, the brightness temperature is insensitive to physical temperature variations in the cloud region. If the specific humidity were held constant, then the brightness temperature would indeed vary directly with the kinetic temperature; however, at constant relative humidity as assumed in the model, the weighting function follows the ammonia as the temperature of the cloud-region atmosphere is varied and tends to stay constant in relation to temperature. There is a small effect, about 1 K of brightness temperature change for a 5 K shift in the adiabat, caused by the corresponding pressure shift with temperature and the effect of this on the absorption model. In view of these considerations we conclude that the radiometric brightness at 2.2 cm depends to first order only on the ammonia distribution, and in particular only on the cloud-level humidity for small departures from the reference model. However, when the cloud-level ammonia becomes highly depleted, the weighting function descends into the subcloud region and the interpretation becomes more complicated. This condition occurs in several important regions in the present maps, and L13 presents a more complete discussion of the implications that the 2.2-cm data hold for the ammonia subcloud distribution in such a case.

3.2. Generating maps

The time-ordered scan data consist of a stream of relative values for the antenna temperatures on the sky and the reference load obtained each second. Maps were produced from these data in a series of steps, which we outline here and illustrate below. To begin, we note that we use the same convention as described in J09 for defining the power collected by the antenna, the "antenna temperature", and the source brightness, or "brightness temperature". In usual practice the antenna temperature, or radiant power collected by the antenna, is the brightness temperature integrated over the whole sky as weighted by a normalized antenna gain pattern; e.g., the antenna temperature of a blackbody distribution over the whole sphere would be the blackbody brightness temperature (cf. Janssen, 1993). In principle the brightness temperature distribution may be determined from measured antenna temperatures by inverting this relationship, subject to a loss of spatial resolution at scales smaller than the main antenna beam. However, we assume here an antenna temperature calibration scale that is normalized over only the measured antenna pattern inside a cutoff angle of 2° where the pattern is well known (see Section 2.2 of J09), with a gain calibration factor applied to the raw radiometer signal as appropriately determined for this convention. It remains then to determine and subtract the sidelobe contributions, after which the correctly scaled brightness distribution is obtained with knowledge of this truncated main beam pattern (henceforth called the TMB). This approach is convenient for the case where the absolute calibration of measurements over an extended source is based on source "ground truth", as was the case for Titan, since residual errors in the knowledge of both the near and far beam pattern are canceled out to first order. For example, the net results were shown in J09 to be insensitive to the exact choice of cutoff angle.

The gain calibration determined for Titan was first directly applied to the raw data on Saturn to convert them to the Kelvin scale without concern for baseline variations, using the above convention for beam normalization. At the same time, the beam pattern was convolved with the brightness temperature distribution of our reference model for the observing geometry of each measurement point to produce a set of model antenna temperatures. As with Titan, the beam pattern convolution was performed separately for the TMB and the far sidelobe pattern (FSL in the following). This convolution took into account the modeled emission-angle variation of the brightness across Saturn and assumed a value of 2.7 K for points off the disk. The model included a simple description of the ring blockage for the FSL convolution, but not for the TMB convolution for reasons discussed later. The cold sky baseline was determined from the excursions off the disk at the end of every scan, using the sum of the TMB and FSL convolutions to correct the baseline for all sidelobe contributions to the off-disk measurements. Specifically, each off-disk excursion was used to estimate a baseline correction to the calibrated data set applicable

for that time, and the offset for all data points was then determined by linear interpolation with time between adjacent baseline estimates. Subtraction of the FSL convolution from all the data then removes this contribution as if it were an error signal, while application of the baseline correction adjusts the data to an absolute scale consistent with our normalization. Subtraction of the TMB convolution over the reference model from this calibrated and baseline-adjusted data set then produces a set of time-ordered residual antenna temperatures, which we interpret as residual brightness temperatures of Saturn relative to the model corrected for both near and far sidelobes. These were then interpolated onto a regular grid in cylindrical coordinates to produce maps. The remainder of this paper deals only with such maps of brightness temperature residuals.

We use the December 2009 mapping campaign as an example to illustrate the steps leading to a set of time-ordered residual brightness temperatures as well as an initial map based on them prior to the removal of remaining systematic errors. The four panels of Fig. 5 show the steps taken to obtain the calibrated and baseline-adjusted antenna temperatures from this campaign. Each 1-s measurement is plotted as a single point in all panels. Top to bottom, the panels show respectively: (a) the time-ordered data on a scale that is calibrated for brightness temperature but uncorrected for a variable offset due to far sidelobe contributions and baseline drift; (b) the individual convolutions over the reference model for Saturn's brightness distribution by the truncated main beam and complementary far sidelobe pattern, labeled TMB and FSL respectively in the right-hand portion of this panel; (c) the zero offset correction for the time-ordered calibrated data derived using the modeled off-disk antenna temperatures and far sidelobe corrections shown in (b); and (d) the final calibrated and baseline-adjusted antenna temperatures obtained by subtracting the zero offset and the far sidelobe contribution from the calibrated data set in (a). The right-hand section of each panel shows a subset of the data on an expanded time scale centered near the center of the pass.

Systematic features seen in these plots are artifacts due to the scan pattern and model assumptions. The ragged signal shown at the base of the measured antenna temperatures in panel (a) is due to the presence of contributions from both near and far sidelobes when the beam axis moves off the disk, with the sawtooth appearance of the minima reflecting the periodic adjustments made in the scan to follow the limb. Panel (b) shows that this pattern is predicted by the modeling. This panel shows two overlying plots representing the separate convolutions of the model by the TMB and FSL patterns. The signal from the latter is observed as the set of points in the middle of the plot smoothly ranging from about 5 K to nearly 25 K. These are largest when the beam approaches the center of the disk, and remain relatively large (7–10 K) even when the beam goes off the disk. The TMB values go to zero when the beam axis moves more than 2° off the disk as seen near the center of the scan, leaving the observed sawtooth pattern where it does not. The baseline in the final adjusted and calibrated data set in panel (d) is seen to correspond to the 2.7 K sky background brightness, while examination of the right-hand plot shows that the scatter of points below this baseline are due to the transition of the beam across the disk edge where the measured signal is sensitive to small pointing errors.

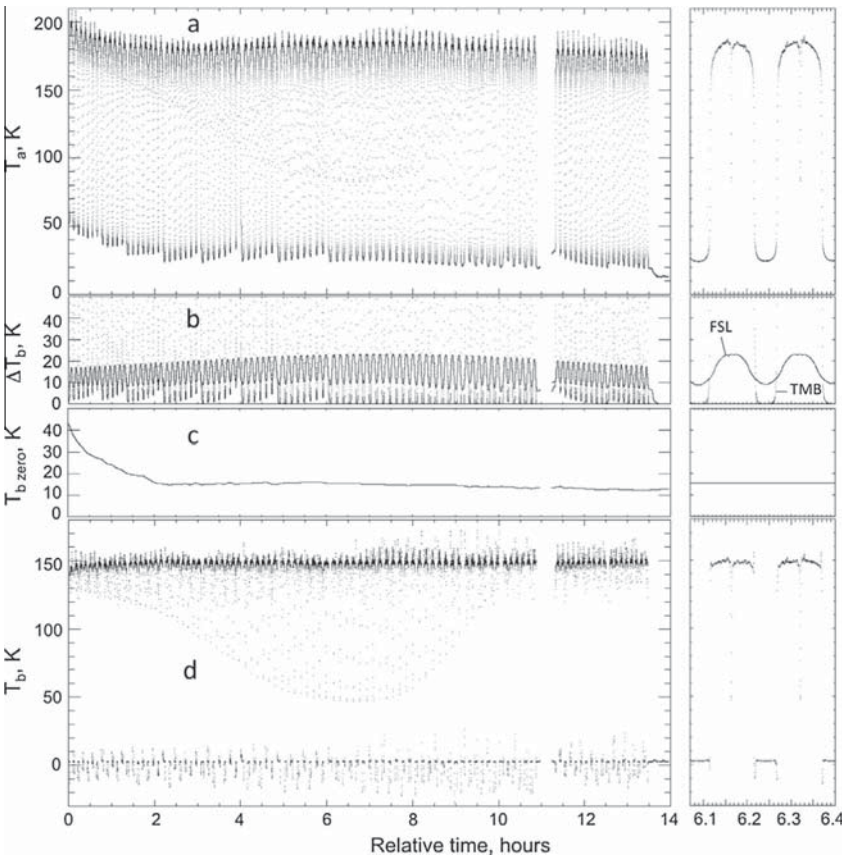

Fig. 5. Initial steps in the calibration process are illustrated for the December 2009 map. Each 1-s measurement from this observing campaign is plotted as a single point in all panels. Top to bottom, the panels show respectively: (a) the time-ordered data with an initial scale calibration but without a baseline correction; (b) model convolutions over the reference model to obtain estimates of the sidelobe contributions; (c) a derived zero offset correction; and (d) the final calibrated and baseline-adjusted antenna temperatures. The right-hand section of each panel shows a subset of the data on an expanded time scale centered near the center of the pass.

The brightness residuals were then used to generate the global cylindrical map shown in Fig. 6. This map was made using the idl TRIANGULATE procedure and TRIGRID function to interpolate the irregularly-spaced time-ordered measurements onto a regular grid with 0.5° spacing, using idl's CONTOUR plotting routine to produce the map. The gray scale was chosen to show the unmeasured portion of the plot as a dark gray corresponding to a residual of 0 K, i.e., as the brightness of the reference model, compared to which the maps points are expected to show a lighter shade. The black region along the equator is due to blockage by the rings, which are mostly optically thick and of much lower brightness than the disk. This and all following maps were cut off beyond an emission angle of 70°, where small errors in pointing begin to dominate the brightness uncertainty.

This map demonstrates the ability of the radiometer to distinguish among small features with brightness variations approaching the 0.1 K white-noise level of the measurements, a capability also demonstrated in the Titan observations. Nevertheless the map contains artifacts with greater brightness variations on large spatial scales that need to be accounted for. The most obvious occurs at the start of the scan at approximately 165° west longitude, where the first 30° or so of the map westward from this appears significantly cooler than the remainder of the map. This is an artifact seen only in the December 2009 map. In all other observations we used a warm-up period of 3 h prior to operations to allow the radiometer to thermally stabilize; however, in this case we were prevented from doing this by a power conflict with a previous (non-RADAR) observation. We elected to start our mapping immediately at RADAR turn-on knowing that our calibration algorithm was not valid for the resulting thermal transient. We in fact see about a 3 K brightness temperature drift in the map, a warm-up effect also apparent in the baseline drift seen in panel (c) of Fig. 5. Another apparent artifact is a striping with longitude, a smaller systematic effect that we ascribe to the incomplete removal of sidelobe signal in the establishment of the baseline.

An artifact not immediately apparent but also important to consider is a low-spatial-frequency brightness error caused by range-related errors in removing the far sidelobe contribution. The solution for the Titan mapping was less dependent on the removal of this error signal because of the way the map mosaic was constructed. The Titan mapping used low-resolution observations made at long range, with small and ultimately accountable far sidelobe contributions, to provide the absolute map level, while observations at closer range were used to provide the higher spatial resolution components. At the same time the far sidelobe contributions were determined from the range-dependent offsets obtained in reconciling near and far-range measurements of the same regions on Titan. The sidelobe pattern was retrieved as part of this reconciliation, for example. This was simplified by assuming it to depend only on polar angle, i.e., to be uniform in azimuth. This process essentially filtered out residual errors associated with the large sidelobe contributions from the close-range measurements, and so was adequate for Titan. This solution left the possibility of residual low-spatial-frequency errors for the Saturn mapping, however, and are estimated based on the J09 analysis to be present at around the 1% level.

We searched for such residual sidelobe contamination in the maps, anticipating that they would appear as systematic errors that depend on spacecraft range and orientation. We took advantage of regions of latitude in both hemispheres in which there is little or no longitudinal structure; in particular, we considered the bands from about 15° to 55° latitude in the north, and −15° to 32° latitude in the south, where no longitudinal structure was discernable in any of the maps except for the northern storm in the 2011 map and the ring blockage in the 2010 map. Excluding the latter, we expected the average brightness across these latitudes to be approximately the same for each scan. Fig. 7 shows the weighted average of these "quiescent" bands in both hemispheres plotted for each scan as a function of elapsed time, with the mean for all scans subtracted to give a zero mean offset. The features in these plots can be associated with the three main sources of error we expect to see. First, the general trend among the plots follows the shape of the respective range curves, which are also plotted and shown as solid lines. This trend indicates an uncorrected sidelobe contribution that varies by as much as 1 K with range, consistent with the ∼1% sidelobe error residual anticipated. Secondly, gain drifts are present, most notably the ∼2% drift seen at the start of the December 2009 mapping campaign. Another possible gain variation is apparent in the third segment of the September 2005 campaign, which is offset by about 1% relative to the average over the same range in the first segment. Thirdly, the remaining scatter may be explained by errors in the baseline correction, caused by a combination of short-term gain drifts and residual errors in the offset modeling. The latter explanation is consistent with the correlation between the patterns in these and the TMB modeling of the off-limb scans in panel (b) of Fig. 5; e.g., compare the upward drift seen in Fig. 7 for the December 2009 plot from about 11 to 12 h to the minima at the same times in the TMB values in panel (b) of Fig. 5.

We also used the quiescent band mean brightness for each map to examine the long-term dependence on gain (or Saturn's mean brightness) with time. The original Titan calibration used a series of measurements of Titan's unresolved disk brightness temperature made from long range to search for gain calibration drift in the measurements (J09). This was reexamined with distant Titan observations obtained through 2012, finding a downward gain drift of 0.2% per year, but barely statistically significant. This rate was incorporated into the present Saturn calibration. Fig. 8 shows the dependence with time on the quiescent band mean brightnesses obtained using this gain drift rate. If correct, this would indicate a steady brightness temperature decrease of Saturn in these quiescent bands, which we consider unlikely. Rather, we take the drift

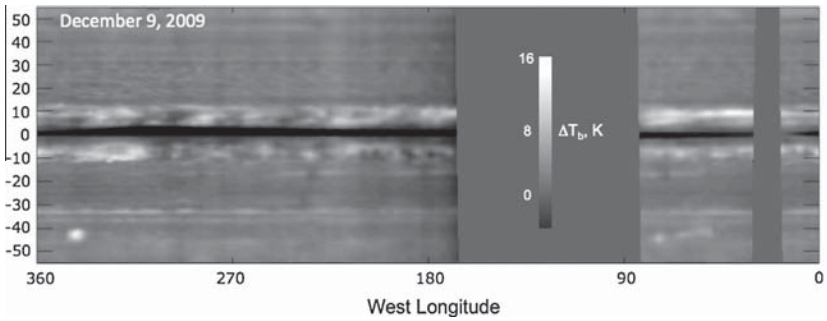

Fig. 6. Global map of brightness temperature residuals from December 2009, before further adjustment to remove artifacts.

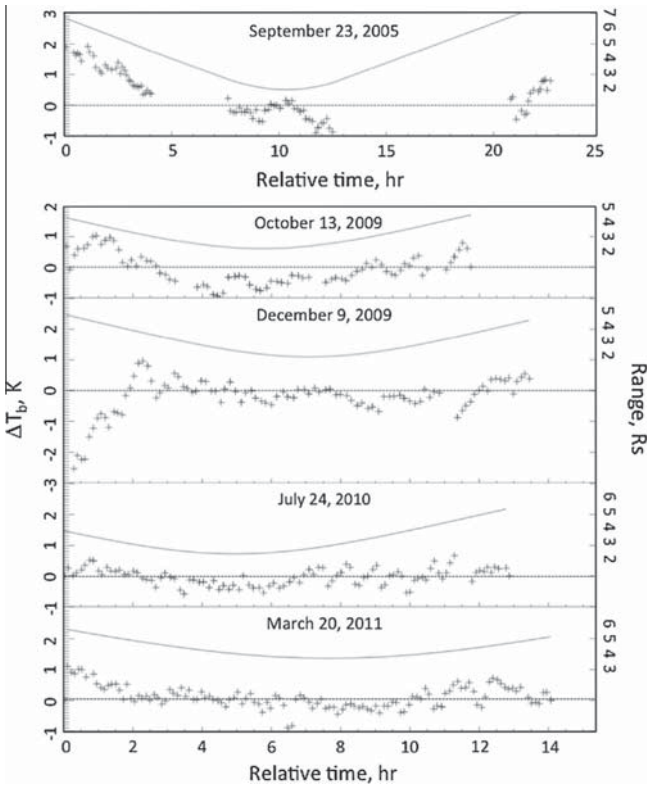

Fig. 7. Mean values by scan of "quiescent" latitudinal bands in northern and southern hemispheres, plotted by elapsed time and compared with range for each map. Each point (+) shows the mean brightness temperatures of each individual scan in these bands, plotted relative to the overall mean, with values given on the left-hand scale. The solid curves show range in units of Saturn radii as given on the right-hand scale.

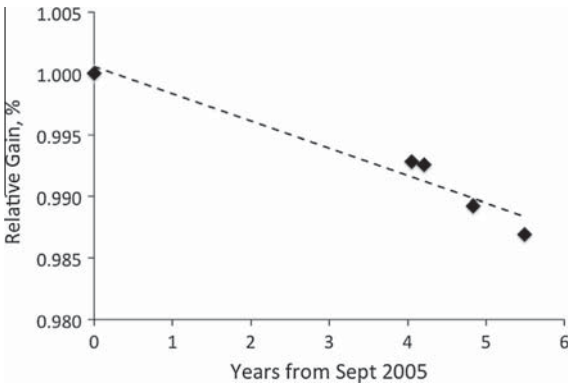

Fig. 8. Values of global mean quiescent band brightness temperatures as described in the text for each calibrated Saturn map relative to that for September 2005. The dashed line is a linear fit that we take to indicate a radiometer gain drift with time.

apparent in Fig. 8 to indicate a net radiometer gain decrease of about 0.4% per year. This is larger than that obtained from the current distant Titan observations, but it is within its error margin and has better precision. We then used this revised rate to adjust each of the maps relative to the epoch valid for the transfer of the Titan absolute calibration from J09.

3.3. The maps

After correcting the data for gain drift, the final residual maps were produced by subtracting the quiescent-band averages of Fig. 7 from each scan in the time-ordered data, using the interpolation described for Fig. 6 to produce the final gridded cylindrical maps shown in Fig. 9. Table 3 supplements these maps by providing details of the map characteristics, which vary with latitude and longitude because of the changing geometry. These maps then represent our best estimates of Saturn's brightness distribution at the times of observation.

We have searched for other sources of error in the mapping but have found nothing of such significance as to warrant further analysis. In principle the steps leading to these maps could be iterated, using the map from one iteration to generate the residuals of the next, continuing until the solution converged on the best estimate of Saturn's brightness temperature distribution consistent with the measurements. However, we find that the solution converges sufficiently well in a second iteration that used Saturn's mean brightness instead of the reference model to recompute and remove the FSL contribution, with remaining uncertainties such as those due to ring blockage limiting the usefulness of further iterations. Fig. 10 shows the brightness temperature distribution with latitude for a single scan across the rings where they were the most open in the July 2010 mapping campaign. The behavior of this blockage with ring inclination could be modeled from the present data and likely contains information about the scattering properties of the rings; however, this is not easily accomplished, and the gain to understanding Saturn's atmosphere was deemed to be small and beyond our scope. In particular, we neglect the contribution from the inner sidelobes of the main beam, which affect the brightness measured within a few beamwidths of the edge of the ring blockage. In the far sidelobe convolution the details of the ring brightness distribution are not important; however, their integrated effect needs to be considered, particularly for the July 2010 map. As an approximation we assumed, for all maps, a constant brightness of 40 K for all inclinations in the region of geometrical blockage. This simple model is sufficient for our purposes; for example, a 10 K error in this value would primarily affect the July 2010 modeling, where it is estimated to lead to an error less than 0.5 K. This being the worst case, we ignore this source of error overall.

The far sidelobe solution for Titan assumed the pattern to be independent of azimuth angle. A possible north–south asymmetry in the far sidelobes could have an impact on the determination of asymmetries between Saturn's northern and southern hemispheres. The scanning used in the three mapping campaigns in 2009 and 2010 inverted the spacecraft rotation axis with respect to Saturn's poles in the final observational segment of each map (see Table 3), however, and this allows us to test for such an artifact. In Fig. 11 we compare the latitudinal dependencies before and after the spacecraft inversion by individually averaging the longitudinal brightness at each latitude. An asymmetry in the pattern would appear in the difference of these averages. We see no sign of such an asymmetry in the figure within the variability caused by real longitudinal brightness structure, which is less than 1 K outside the active latitudes and regions of ring blockage. A systematic polar angle error in this pattern is not detected by this approach, however, and remains possible in the range-dependent signal seen in Fig. 7. We anticipate that an uncompensated systematic error as large as 1 K that is symmetric around the equator could be present based on studies described in J09.

The absolute calibration for Titan was determined to be about 1% in J09. This result is confirmed and improved by current work in progress, although here we claim only the calibration accuracy described in detail by J09. The transfer of this calibration to Saturn involves additional uncertainties that follow from the steps described above. A range-dependent effect on the order of 1% was anticipated in the Titan calibration process, and is apparent in

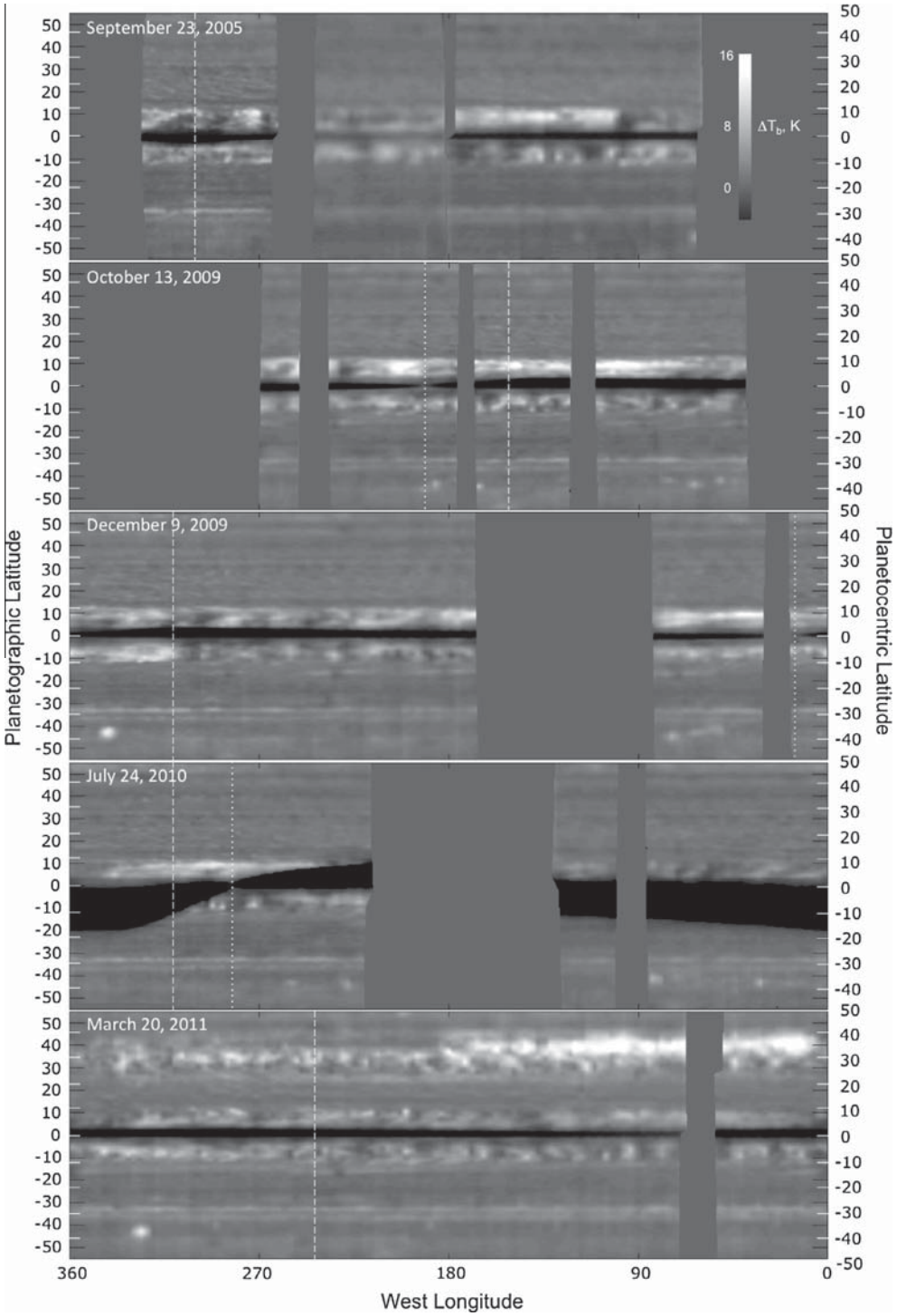

Fig. 9. Final cylindrical maps of Saturn from the five observation campaigns. The absolutely calibrated maps are shown in the five panels as residuals from a model that assumes ammonia to be fully saturated in the cloud-forming region. The dashed and dotted lines indicate periapsis and ring plane crossings, respectively (there were no observations made exactly at ring plane crossing for the 2005 and 2011 maps). Planetographic latitudes are indicated by black ticks on the vertical scales, planetocentric by white. The unobserved portions of the maps are shaded to the equivalent brightness for the fully saturated model, so that, except for the ring blockage around the equator, the maps indicate that the ammonia cloud region is everywhere unsaturated. Orbital characteristics and mapping details are given in Tables 2 and 3, and uncertainties and caveats concerning the maps are given in the text.

Fig. 7 with a value ranging over about ±0.5%. Errors in the removal of gain as well as sidelobe signal variations using the quiescent-band averages will lead to errors as well, which we judge to be relatively small by examining the time dependence of these averages in Fig. 8. Conservatively, we expect an absolute uncertainty better than 2%, or a brightness temperature uncertainty less than 3 K. Large-scale systematic errors are smaller, perhaps as much as 1 K from equator to pole as discussed above, and <1 K elsewhere Small-scale errors are consistent with the white noise of the individual measurements, ~0.1 K.

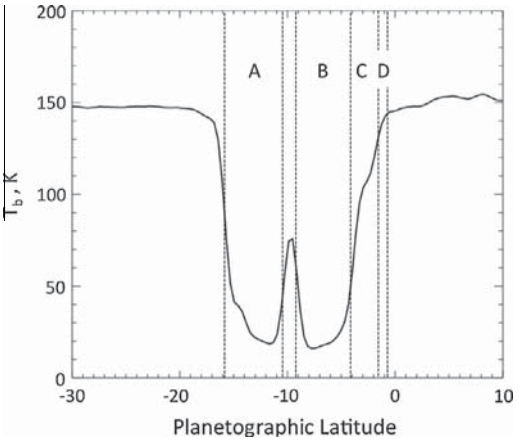

Fig. 10. Brightness distribution through the region of ring blockage. The calibrated brightness temperature is shown for one scan in latitude around the time of peak ring inclination with respect to the spacecraft in the July 2010 mapping campaign. The boundaries between the rings are indicated. The Cassini Division is clearly seen.

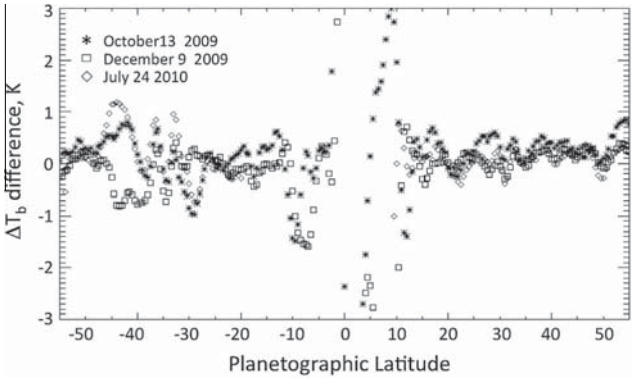

Fig. 11. Differenced longitudinal averages of the latitudinal brightness distribution for the three maps in which the spacecraft *Y*-axis was inverted partway through the observation. The longitudinal brightness at each 0.5° in latitude was averaged separately for the two orientations and subtracted to search for an asymmetry in the N–S sidelobe pattern. None is apparent.

4. Discussion

The maps in Fig. 9 reveal features either never before seen or known features viewed from a perspective never before available. The region of the atmosphere responsible for the microwave brightness variations, ~0.5–2 bars, has been extensively observed with high-resolution instruments at infrared wavelengths. Nevertheless, the unique value of observations at 2.2-cm wavelength is the simple origin of the observed structure – it is just ammonia vapor and variations in its distribution. Low residual brightnesses indicate the presence of gas phase ammonia in the cloud region at concentrations approaching but not exceeding its saturation level, whereas higher brightnesses indicate depletion relative to this. The variability of the brightness distribution across Saturn suggests the existence of circulations that cause the depletion or enhancement of the ammonia by means of gas flow into and out of the ammonia condensation region, while the morphologies of these variations give clues as to the nature of the dynamical forcing causing these flows. Obvious features include the bright bands that are symmetric about the equator from approximately 3° to 10° latitude north and south respectively, where regions of high brightness alternate with low brightness regions resulting in longitudinal variability not seen at higher latitudes until the great northern storm in the 2011 map. The regions of high brightness in these bands are "dry" in the sense of low ammonia abundance, and therefore resemble the dry sub-tropics of Earth. They are perhaps indicative of the convective organization of planetary waves similar to related pervasive features within the Earth's tropics and the 11–13 wavenumber plumes and 5-μm hot spots on Jupiter (Allison, 1990; Arregi et al., 2006).

In between these bands, at the equator, is a central band of relative calm with the lowest brightness seen on Saturn. The low brightness seen here indicates ammonia concentration to be near saturation, consistent with the greatly enhanced NH_3 abundances found by VIMS in this region (Fletcher et al., 2011). Although difficult to discern because of the ring blockage, this band is apparent at or near the ring crossings, most notably in the central segment of the 2005 map. Although at relatively low resolution, the ring inclination in this segment is near 0.01° as seen from the spacecraft, with the blockage causing less than a 1 K influence on the brightness. L13 presents a more thorough examination of the ring blockage, using a ring model to retrieve the equatorial brightnesses at the ring plane crossings for all maps to confirm the presence generally of near-saturated ammonia in the equatorial belt.

Relatively strong narrow bands with less longitudinal structure are seen in the south at −33° and −37° latitude. The northern latitudes show milder banding (until the eruption of the great northern storm) with little similarity to the southern hemisphere. A major feature seen in the southern hemisphere is a series of large circular bright features between −42° and −47° latitude. These are apparently related to lightning storms observed at optical and infrared wavelengths (Porco et al., 2005). They appear just south of the westward jet at −41° (−35° planetocentric) latitude (Sanchez-Lavega et al., 2000). Their development and life cycle is uncertain and likely complex. In methane band images they first appear as high, thick clouds with irregular, convective morphology. Baines et al. (2009) see spectroscopically-identifiable ammonia clouds first appearing in association with lightning, followed by the emergence of dark clouds that are optically-thick at 5 μm with a spectrum consistent with dark carbon soot. Meanwhile, Dyudina et al. (2007) report their emergence after a few days as circular spots with only a thin haze over a cloud-free deep atmosphere (see her Figs. 3 and 4). At the stage we see them (possibly later in their development) they have become relatively extensive areas that are depleted in ammonia, likely well below the ammonia condensation level (see L13).

The great northern storm appearing in the 2011 map is depicted again in Fig. 12 with a shading stretch that better shows its structure, along with the beam footprints to illustrate the spatial resolution in this image. Overall, this is a brighter and more widespread feature than seen elsewhere in any of the maps. There are a few regions elsewhere that show peak residuals as high as seen throughout the storm, but these are localized (e.g., occasional spots in the equatorial storm bands) and likely represent extremes for a relatively weaker class of feature. The 2011 image of the great northern storm indicates the depletion of ammonia on much larger scales than seen in the other maps. Implications of this for atmospheric processes at work are discussed further in L13.

Fig. 13 shows the latitudinal structure and its variability with time for all maps. Each point represents the unweighted average of the brightness residuals in each map at 0.5° increments of latitude. With the exception of unobserved regions, all values are included irrespective of ring blockage, etc. The overall latitudinal structure in this representation shows a remarkable degree of repeatability, apart from the readily apparent ring blockage in the equatorial region and the singular effect of the 2011 storm. A north–south asymmetry is evident in both brightness and structure. The narrow bright bands and circular bright features dominate the southern structure, while the northern midlatitudes

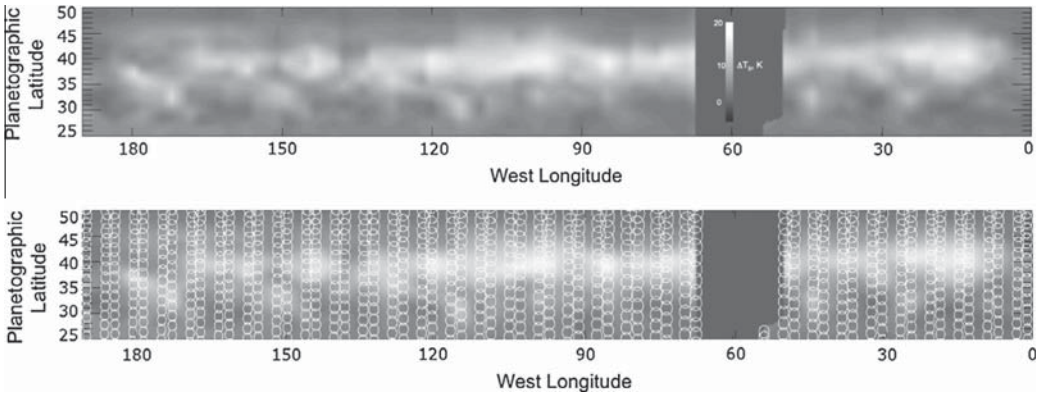

Fig. 12. The great northern storm of 2010. The section of the March 2011 map containing the storm is shown in the upper panel with a stretch that enhances the high brightness regions. The lower panel gives the half-power footprints (showing only every fourth footprint in latitude).

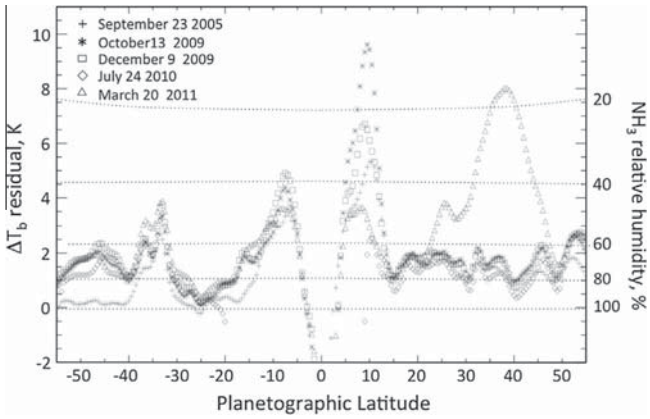

Fig. 13. Longitudinal averages of the latitudinal brightness distribution for all maps. The equatorial region within 5° is generally dominated by ring blockage, as is the region from −20° to 0° for the July 2010 map – the plunge to negative residuals in these regions is an artifact of this. The dotted lines indicate model brightness residuals that would be observed if cloud relative humidity were allowed to vary relative to the fully saturated model.

show repetitive banding at approximately 10° spacing. Residual brightness temperatures in the region from about −15° to −30° are almost as low as those in the central equatorial band inside 3°. Finally, the north equatorial band from 3° to 10° shows significant variability, while its southern counterpart appears relatively constant. We have no simple explanation for the asymmetries we see. These may have to do with seasonal variations, or may reflect some degree of chaos in Saturn's large-scale circulations. For example, Jupiter has a small obliquity compared to Saturn, but has demonstrated considerable and apparently chaotic variability in belt-zone structure over the decades. Seasonal shadowing by Saturn's rings resulting from its large obliquity could lead to seasonal variations between hemispheres if solar forcing were significant in driving circulations. We call attention to the structural asymmetry in the banding apparent in the maps of Fig. 9 from approximately 10° to 30° latitude, best seen in the high-resolution segment of the 2005 map. The southern hemisphere in this region shows faint but discernably regular banding, while the northern counterpart appears mottled. The latter was in the ring shadow in 2005 and the irregular appearance may reflect a lack of solar forcing.

We use a simple variation on our reference model to illustrate the dependence of the brightness residuals on ammonia distribution in this figure. As in the reference model we assume a constant deep ammonia mixing ratio of 3 × solar, however, above its condensation level we assume a constant relative humidity, the value of which we allow to vary (this is equivalent to the parameter DF_{cb} in L13). For example, the light solid line in Fig. 4 shows such a case for a cloud relative humidity of 50%. The dotted lines in Fig. 13 show the brightness then expected for a given cloud relative humidity, which varies weakly as a function of the viewing geometry and is aliased closely with latitude. Our immediate interpretation is that most of the brightness structure seen throughout the maps can be explained by varying ammonia concentrations in the cloud region alone. The exceptions are the equatorial bright bands bracketing the equator, the circular bright features seen between −42° and −47° latitude, and the northern storm in the 2011 map, all of which have regions that cannot be explained unless subcloud ammonia is depleted as well. The companion paper L13 considers the effect of subcloud mixing ratios using a more realistic model involving both cloud-level and subcloud variations in ammonia concentration.

5. Conclusions

The advantage of proximity gained from a spacecraft platform has enabled a significant advance to be made in observing Saturn in the microwave region. Earth-based platforms such as the VLA and more recent millimeter and submillimeter arrays have provided the best imaging results on Saturn prior to this work, but their capabilities are limited by the aperture synthesis approach they require. Although theoretically capable of higher spatial resolution and sensitivity, reported VLA images of Saturn in the centimeter-wavelength region show 0.9 arcsec resolution at best, equivalent to ∼6° latitude at the equator, with brightness temperature sensitivity >1 K. Broad latitudinal banding has been observed under these conditions, and the use of multiple frequencies has enabled useful interpretations of the distribution of absorbers (Grossman et al., 1989; Grossman, 1990; van der Tak et al., 1999). However, longitudinal structure on rotating planets is difficult to obtain by aperture synthesis, and has never been attempted for Saturn. The present maps resolve latitudinal structure as small as 1° and longitudinal structure to 2°, a significant improvement. Our absolute calibration of 2% represents an improvement by at least a factor of two as well. The sensitivity for features on small scales, as good as 0.1%, appears to be over an order of magnitude better, while the largest remaining source of error is the possibility of a systematic error of ∼1 K that is symmetric about the equator.

As a result we see structure at resolutions approaching those achieved by ground-based optical and infrared telescopes, and begin to identify features that appear related to those seen both from ground and space at these shorter wavelengths. Our 6-year baseline and excellent stability allows us to contribute to the

question of Saturn's long-term stability. We find that Saturn's brightness has been remarkably stable over this period at most latitudes, with variations much less than 1%. Exceptions include the north equatorial bright band, possibly the southern storm alley around −45° latitude, and the great storm in the March 2011 map. These contrast with time variability seen by the VLA in the late 1980s and early 1990s, where van der Tak et al. (1999) report substantial latitudinal brightness variations in both hemispheres. We also see a southern hemisphere that is somewhat (~1%) cooler than the north, while van der Tak et al. see a southern hemisphere from 1990 to 1995 that was brighter than the northern by 5%, at wavelengths of 2 and 6 cm. Some of the variability may be due to the different wavelengths used and the insensitivity of the 2.2-cm emission to atmospheric temperature and subcloud ammonia variations; however, the 2-cm VLA banding seen earlier by van der Tak et al. is clearly different than the 2005–2011 results presented here and implies the existence of long-term variability in our "quiescent" bands. For example, a storm equivalent to the 2010–2011 storm might have been present in the southern hemisphere at that time. Unlike the northern storm, however, it must have persisted for 5 years to explain the observations, which we consider unlikely. One more global equatorial map is planned for 2015, which will extend our time base to 10 years if successful, allowing us to further address the question of long-term variability. Finally, improvements to the VLA and the coming on-line of new millimeter-wavelength arrays should enable this question to be pursued for many more years, using the present results as a baseline.

We have limited our interpretation to that allowed by the present observations themselves, noting that L13 goes more thoroughly into interpretations involving both the horizontal the vertical ammonia distribution and relates them to dynamical models for the circulations. We also remark that the 2.2-cm radiometric mapping campaign was part of a combined effort with the Visual Infrared Mapping Spectrometer (VIMS) on Cassini that was begun after the 2005 radiometer mapping effort proved successful. This consisted of VIMS observations of the same regions imaged by the microwave radiometer both before and after the pass so that wind-corrected overlays of the infrared maps with the microwave maps could be examined. Since the VIMS instrument observes the same pressure range of the atmosphere but is affected by other constituents (clouds and haze in particular), questions concerning circulations and related processes can be examined more fully. Work is currently in progress to compare the VIMS and microwave mapping. Further, the calibrated data and derived maps from the present work have been submitted to the Atmospheres Node of the Planetary Data System and will be available for comparative studies in general around the time of the publication of this paper. Lastly, interpretations of the present results are limited because only one frequency was used. Improved VLA capabilities and future missions using multiple microwave frequencies can achieve much more in understanding the deep circulations and vertical structure of the microwave-active constituents ammonia and water. For example, the Juno mission currently on route for arrival at Jupiter in 2016 carries a six-frequency microwave radiometer that will observe Jupiter's deep atmosphere to pressures greater than 100 bars with such a goal (Janssen et al., in preparation).

Acknowledgments

This research was conducted at the Jet Propulsion Laboratory (JPL), California Institute of Technology, under contract with the National Aeronautics and Space Administration (NASA). It is partly based upon work supported by NASA under Grant No. 10-CDAP10-0051 issued through the Cassini Data Analysis and Participating Scientist (CDAPS) Program. We acknowledge Sushil Atreya, Lena Adams, and Virgil Adumantroi for their invaluable contributions to the Juno Atmospheric Microwave Radiative Transfer (JAMRT) program, P. Steffes for discussions on the microwave absorption of ammonia in the Saturn atmosphere, Scott Bolton, Steve Levin, and the Juno project for their encouragement of this work, Alice Le Gall for her contributions to the calibration, Bryan Butler for discussion of the capabilities of ground-based interferometers, and Glenn Orton for useful discussions on sources of microwave absorption as well as related visual and infrared observations of giant planet atmospheres. We also gratefully acknowledge the Cassini RADAR team in general for their support, along with those who designed, developed and operate the Cassini/Huygens mission, which is a joint endeavor of NASA, the European Space Agency (ESA), and the Italian Space Agency (ASI) and is managed by JPL/Caltech under a contract with NASA.

References

Allison, M., 1990. Planetary waves in Jupiter's equatorial atmosphere. Icarus 83, 282–307.

Arregi, J. et al., 2006. Phase dispersion relation of the 5-micron hot spot wave from a long term study of Jupiter in the visible. J. Geophys. Res. 111, E09010. http://dx.doi.org/10.1029/2005JE002653.

Atreya, S.K., 1986. Atmospheres and ionospheres of outer planets and their satellites. Springer-Verlag.

Atreya, S.K., 2010. Atmospheric moons Galileo would have loved. In: Galileo's Medicean Moons – Their Impact on 400 Years of Discovery. Cambridge University Press, pp. 130–140 (Chapter 16).

Baines, K.H. et al., 2009. Storm clouds on Saturn: Lightning-induced chemistry and associated materials consistent with Cassini/VIMS spectra. Planet. Space Sci. 57, 1650–1658.

Berge, G.L., Gulkis, S., 1976. Earth-based radio observations of Jupiter: Millimeter to meter wavelengths. In: Gehrels, T. (Ed.), Jupiter. Univ. of Arizona Press, Tucson, pp. 621–692.

Birnbaum, G., Borysow, A., Orton, G.S., 1996. Collision-induced absorption of H_2–H_2 and H_2–He in the rotational and fundamental band for planetary applications. Icarus 123, 4–22.

Borysow, A., Frommhold, L., 1986. Theoretical collision-induced rototranslational absorption spectra for the outer planets: H_2–CH_4 pairs. Astrophys. J. 304, 849–865.

Briggs, F.H., Sackett, P.D., 1989. Radio observations of Saturn as a probe of its atmosphere and cloud structure. Icarus 80, 77–103.

Cottini, V. et al., 2012. Spatial and temporal variations in Titan's surface temperature from Cassini CIRS observations. Planet. Space Sci. 60, 62–71.

de Pater, I., 1990. Radio images of the planets. Annu. Rev. Astron. Astrophys. 28, 347–399.

de Pater, I., Dickel, J.R., 1982. New information on Saturn and its rings from VLA multifrequency data. In: Proceedings of Planetary Rings/Anneaux des Planetes Conference, Toulouse, France, August 1982 (abstract).

de Pater, I., Dickel, J.R., 1991. Multifrequency radio observations of Saturn at ring inclination angles between 5° and 26°. Icarus 94, 474–492.

de Pater, I., Massie, S.T., 1985. Models of the millimeter–centimeter spectra of the giant planets. Icarus 62, 143–171.

de Pater, I., Dunn, D., Zahnle, K., Romani, P.N., 2001. Comparison of Galileo probe data with ground-based radio measurements. Icarus 149, 66–78.

Deboer, D.R., Steffes, P.G., 1994. Laboratory measurements of the microwave properties of H_2S under simulated jovian conditions with an application to Neptune. Icarus 109, 352–366.

Deveraj, K., 2011. The Centimeter- and Millimeter-Wavelength Ammonia Absorption Spectra under Jovian Conditions. Ph.D. thesis, Georgia Institute of Technology, Atlanta.

Dunn, D.E., Molnar, L.A., Fix, J.D., 2002. More microwave observations of Saturn: Modeling the ring with a Monte Carlo radiative transfer code. Icarus 160, 132–160.

Duong, D., 2011. The Complex Dielectric Properties of Aqueous Ammonia from 2 GHz to 8.5 GHz in Support of the NASA Juno Mission. M.S. Thesis, Georgia Institute of Technology, Atlanta, GA.

Dyudina, U.A., Ingersoll, A.P., Ewald, S.P., Porco, C.C., Fischer, G., Kurth, W., Desch, M., Del Genio, A., Barbara, J., Ferrier, J., 2007. Lightning storms on Saturn observed by Cassini ISS and RPWS during 2004–2006. Icarus 190, 545–555.

Elachi, C. et al., 2004. RADAR: The Cassini Titan radar mapper. Space Sci. Rev. 115, 71–110.

Fletcher, L.N., Baines, K.H., Momary, T.W., Showman, A.P., Irwin, P.G.J., Orton, G.S., Roos-Serote, M., Merlet, C., 2011. Saturn's tropospheric composition and clouds from Cassini/VIMS 4.6–5.1 μm nightside spectroscopy. Icarus 214, 510–533.

Fulchignoni, M. et al., 2005. Titan's physical characteristics measured by the Huygens Atmospheric Structure Instrument (HASI). Nature 438, 785–791.

Grossman, A.W., 1990. Microwave Imaging of Saturn's Deep Atmosphere and Rings. Ph.D. thesis, California Institute of Technology.

Grossman, A.W., Muhleman, D.O., Berge, G.L., 1989. High resolution microwave observations of Saturn. Science 245, 1211–1215.

Gulkis, S., Poynter, R., 1972. Thermal radio emission from Jupiter and Saturn. Phys. Earth Planet. Interiors 6, 36–43.
Gulkis, S.R., McDonough, T.R., Craft, H., 1969. The microwave spectrum of Saturn. Icarus 10, 421–427.
Hanley, T.R., Steffes, P.G., Karpowicz, B.M., 2009. A new model of the hydrogen and helium broadened microwave opacity of ammonia based on extensive laboratory measurements. Icarus 202, 316–335.
Hoffman, J.P., Steffes, P.G., DeBoer, D.R., 2001. Laboratory measurements of the microwave opacity of phosphine: Opacity formalism and application to the atmospheres of the outer planets. Icarus 152, 172–184.
Janssen, M.A., 1993. An introduction to the passive microwave remote sensing of atmospheres. In: Janssen, M. (Ed.), Atmospheric Remote Sensing by Microwave Radiometry. Wiley & Sons, New York, pp. 1–35 (Chapter 1).
Janssen, M.A., Hofstadter, M.D., Gulkis, S., Ingersoll, A.P., Allison, M., Bolton, S.J., Kamp, L.W., 2005. Microwave remote sensing of Jupiter's atmosphere from an orbiting spacecraft. Icarus 173, 447–453.
Janssen, M.A., Lorenz, R.D., West, R., Paganelli, F., Lopes, R.M., Kirk, R.L., Elachi, C., Wall, S.D., Johnson, W.T.K., Anderson, Y., Boehmer, R.A., Callahan, P., Gim, Y., Hamilton, G.A., Kelleher, K.D., Roth, L., Stiles, B., Le Gall, A.the Cassini Radar Team, 2009. Titan's surface at 2.2-cm wavelength imaged by the Cassini RADAR radiometer: Calibration and first results. Icarus 200, 222–239.
Jennings, D.E. et al., 2009. Titan's surface brightness temperatures. Astrophys. J. 691, L103–L105.
Karpowicz, B.M., Steffes, P.G., 2011a. In search of water vapor on Jupiter: Laboratory measurements of the microwave properties of water vapor under simulated jovian conditions. Icarus 212, 210–213.
Karpowicz, B.M., Steffes, P.G., 2011b. Corrigendum to "In search of water vapor on Jupiter: Laboratory measurements of the microwave properties of water vapor under simulated jovian conditions" [Icarus 212 (2011) 210–213]. Icarus 214, 783.
Klein, M.J., Gulkis, S., 1978. Jupiter's atmosphere: Observations and interpretation of the microwave spectrum near 1.25-cm wavelength. Icarus 35, 44–60.
Laraia, A., Ingersol, A.P., Janssen, M.A., Gulkis, S., Oyafuso, F.A., Allison, M.D., 2013. Analysis of Saturn's thermal emission at 2.2-cm wavelength: Spatial distribution of ammonia vapor. Icarus, this issue.
Lindal, G.F., Sweetnam, D.N., Eshleman, V.R., 1985. The atmosphere of Saturn: An analysis of the Voyager radio occultation measurements. Astron. J. 90, 1136–1146.
Lorenz, R.D., 1998. Preliminary measurements of the cryogenic dielectric properties of water-ammonia ices: Implications for radar observations of ice satellites. Icarus 136, 344–348.
Mayer, C.H., McCullough, T.P., Sloanaker, R.M., 1958. Observations of Mars and Jupiter at a wavelength of 3.15 cm. Astrophys. J. 127, 11–16.
Mohammed, P., 2004. Laboratory measurements of the W band (3.2 mm) properties of phosphine (PH_3) and ammonia (NH_3) under simulated conditions of the outer planets. J. Geophys. Res. 109, 1–9.
Orton, G., Gustafsson, M., Burgdorf, M., Meadows, V., 2007. A revised ab initio model for collision-induced H_2–H_2 absorption. Icarus 189, 455–459.
Porco, C.C. et al., 2005. Cassini imaging science: Initial results on Saturn's atmosphere. Science 307, 1243–1247.
Sanchez-Lavega, A., Rojas, J.F., Sada, P.V., 2000. Saturn's zonal winds at cloud level. Icarus 147, 405–420.
Schloerb, F.P., Muhleman, D.O., Berge, G.L., 1979. Interferometric observations of Saturn and its rings at a wavelength of 3.71 per cm. Icarus 39, 214–231.
Thornton, D.D., Welch, W.J., 1963. 8.35 mm radio emission from Jupiter. Icarus 2, 228–232.
van der Tak, F., de Pater, I., Silva, A., Millan, R., 1999. Time variability in the radio brightness distribution of Saturn. Icarus 142, 125–147.
West, R. et al., 2009. Cassini RADAR sequence planning and instrument performance. IEEE Trans. Geosci. Remote Sensing 47, 1777–1795.
Wrixon, G.T., Welch, W.J., 1970. The millimeter wave spectrum of Saturn. Icarus 13, 163–172.